Physics Informed Neural Network-based High-frequency Modeling of Induction Motors

Zhenyu Zhao[1], *Fei Fan*[1*], *Quqin Sun*[2], *Huamin Jie*[1], *Zhou Shu*[1], *Wensong Wang*[1] *and Kye Yak See*[1]
(1. School of Electrical and Electronic Engineering,
Nanyang Technological University, Singapore 639798, Singapore;
2. Science and Technology on Thermal Energy and Power Laboratory,
Wuhan Second Ship Design and Research Institute, Wuhan 430000, China)

Abstract: The high-frequency (HF) modeling of induction motors plays a key role in predicting the motor terminal overvoltage and conducted emissions in a motor drive system. In this study, a physics informed neural network-based HF modeling method, which has the merits of high accuracy, good versatility, and simple parameterization, is proposed. The proposed model of the induction motor consists of a three-phase equivalent circuit with eighteen circuit elements per phase to ensure model accuracy. The per phase circuit structure is symmetric concerning its phase-start and phase-end points. This symmetry enables the proposed model to be applicable for both star- and delta-connected induction motors without having to recalculate the circuit element values when changing the motor connection from star to delta and vice versa. Motor physics knowledge, namely per-phase impedances, are used in the artificial neural network to obtain the values of the circuit elements. The parameterization can be easily implemented within a few minutes using a common personal computer (PC). Case studies verify the effectiveness of the proposed HF modeling method.

Keywords: Equivalent circuit, high-frequency (HF) modeling, induction motor, parameterization, physics informed neural network

1 Introduction

Motor drive systems have been widely used in numerous applications to their excellent power conversion efficiencies. A typical motor drive system, composed of a drive feeding an induction motor through a cable, is shown in Fig. 1. Pulse-width modulation (PWM) pulses in the drive travel across the cable, causing wave propagation effects [1]. The mismatch between the cable characteristic impedance and motor input impedance generates successive voltage reflections, causing overvoltage ringing at the motor terminals [2]. The overvoltage can result in accelerated aging or even failure of the motor winding insulation [3]. Moreover, the fast switching of semiconductors in the drive leads to conducted emissions [4-5], such as the flow of the common-mode (CM) and differential-mode (DM) currents between the drive and motor [6-7]. These conducted emissions may disturb nearby sensitive equipment by various means, such as crosstalk [8] and common-ground interference [9]. High-frequency (HF) modeling of the motor plays a vital role in predicting the motor terminal overvoltage and conducted emissions in a motor drive system [10]. Accurate predictions of these undesired HF phenomena provide valuable input for the optimal design of mitigation methods.

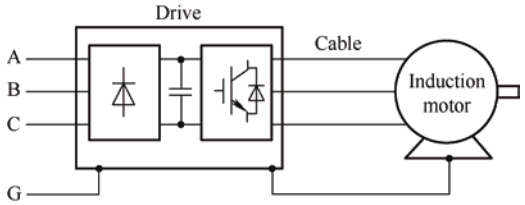

Fig. 1 Typical motor drive system

HF models of induction motors can be categorized into two main types: numerical models [11-14] and behavioral models [15-19]. The former are created by numerical methods such as finite element analysis (FEA), whereas the latter are developed based on the

Manuscript received October 20, 2022; revised November 10, 2022; accepted November 21, 2022. Date of publication December 31, 2022, date of current version December 9, 2022.

* Corresponding Author, E-mail: fanf0003@e.ntu.edu.sg

Digital Object Identifier: 10.23919/CJEE.2022.000036

motor impedance measurements and curve-fitting techniques. Because numerical models can be created in the initial design stage before the motor is fabricated, they are often used to early assess the impact of motor design decisions on undesired HF phenomena [14]. The prerequisite for building a numerical model is obtaining the motor geometry and material properties. However, in view of the motor complexity, it is difficult to obtain accurate details of the motor to establish a high-precision numerical model. Therefore, the accuracy of numerical models is often limited [20]. In contrast, although behavioral models are applicable only when accessing measurement data from a fabricated motor, they usually exhibit higher accuracies than numerical models [12]. Additionally, motor geometry and material properties are not required for behavioral modeling. Behavioral models [21-23] are often used to predict undesired HF phenomena (i.e., overvoltage and conducted emissions) so that mitigation measures (e.g., dv/dt filter [18] and electromagnetic interference filter [16]) can be optimally designed. In addition, they can also be used to evaluate the HF performance of different candidate motors in the construction stage of a motor drive system, realizing fast and appropriate motor selection.

Behavioral models can be further divided into frequency-domain (FD) models [15-17], and circuit-based models [18-22]. FD models are non-circuit-based models that are typically represented using either directly measured motor impedance characteristics over the frequency range of interest or a frequency-dependent matrix fitted from the measured motor impedance characteristics. Circuit-based models use an equivalent circuit to fit the measured motor impedances. FD models are typically used for conducted emissions in the frequency domain. An inherent flaw of FD models is their unsuitability for time-domain applications. In contrast, circuit-based models allow both time- and frequency-domain analysis; therefore, they can be used not only to predict motor terminal overvoltage but also to predict conducted emissions in a motor drive system.

Many circuit-based models have been proposed. Some of them are applicable to both star- and delta-connected induction motors [18-19, 21]. However, these models are often validated only up to 10 MHz. In addition, their circuit element values usually need to be recalculated when changing the motor connection from star to delta, and vice versa. Although there are some other models valid up to 30 MHz, they are often validated only for star-connected induction motors [20, 22]. Because high-precision models in a wider frequency range require more circuit elements, traditional parameterization based on analytical methods is difficult and complex [24]. Some studies have simplified the parametrization process using genetic algorithms [25] or the Monte Carlo algorithm [26]; however, they have only been validated with star-connected induction motors.

In this study, a physics informed neural network-based HF modeling method is proposed. The proposed model of the induction motor consists of a three-phase equivalent circuit, which is an improved form of that reported in Ref. [21]. Compared with the circuit-based model in Ref. [21], more circuit elements were added to each phase to ensure model accuracy over a wider frequency range. Moreover, the per-phase circuit structure is revised to be symmetric with respect to its phase start and phase-end points. This symmetry enables the proposed model to be applicable to both star- and delta-connected induction motors without having to recalculate the circuit element values when changing the motor connection from star to delta and vice versa [24]. Motor physics knowledge, namely, per-phase impedances, are used in the artificial neural network to obtain the values of the circuit elements. The parametrization process can be easily implemented within a few minutes using a common personal computer (PC).

It should be noted that a preliminary version of this work was recently presented at a conference [27]. It predicted the CM and DM impedances of a star-connected induction motor in the range of 100 kHz to 10 MHz. The major improvements of this study over the conference paper [27] are as follows: first, more circuit elements have been added to each phase to ensure model accuracy in a wider range of 1 kHz-30 MHz; second, a symmetric per-phase circuit structure has been used to expand the model versatility, making it applicable for both star- and delta-connected induction motors without having to recalculate the circuit element values when changing the motor

connections; third, the loss function of the neural network has been improved to obtain better training results. The main contribution of this study is the proposal of a motor HF modeling method with the merits of high accuracy, good versatility, and simple parameterization simultaneously.

The rest of this paper is organized as follows. Section 2 describes the motor HF modeling method based on a physics informed neural network. In Section 3, the effectiveness and advantages of the proposed HF modeling method are demonstrated using a 5.5 kW induction motor. Finally, Section 4 concludes the paper.

2 Physics informed neural network-based HF modeling of induction motors

2.1 Reference and proposed models

As mentioned in Section 1, the proposed model is an improved form of the model reported in Ref. [21]. Fig. 2 shows the per-phase equivalent circuit of the model in Ref. [21], which consists of ten circuit elements. L_c is the combined inductance of the stator leakage inductance in the first few turns of the slot and the inductance of the motor's internal feed conductors to the stator winding. C_{g1} and C_{g2} are the equivalent phase-to-ground and neutral-to-ground parasitic capacitances, respectively. R_{g1} and R_{g2} are the equivalent copper skin and proximity-effect resistances. L_s is the stator-winding leakage inductance. R_e denotes the HF eddy-current losses of the stator core. Elements R_t, L_t, and C_t are used to represent the stator winding interturn capacitance effect. For the three-phase equivalent circuit, it is constructed using three per-phase equivalent circuits in Fig. 2 based on a universal star-connected structure, which remains fixed for various motor connections.

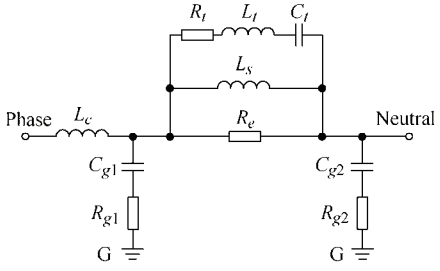

Fig. 2 Per phase equivalent circuit of the model in Ref. [21]

Because of the limited number of circuit elements per phase, the model in Ref. [21] was validated up to only 10 MHz, which is insufficient for applications related to conducted emissions analysis because many electromagnetic compatibility (EMC) standards have mandatory requirements for emissions in a frequency range of up to 30 MHz. To expand the applicable frequency range of the model to 30 MHz, more circuit elements were added to each phase. In addition, the per-phase circuit structure is revised to be symmetric with respect to its phase-start and phase-end points. The per-phase symmetry property of the proposed model enables it to be applicable for both star and delta connections without having to recalculate the circuit element values when changing the motor connection from star to delta, and vice versa [24]. Fig. 3 shows the per-phase equivalent circuit of the proposed model, whose additional circuit elements, in contrast with Fig. 2, are labeled with a prime symbol.

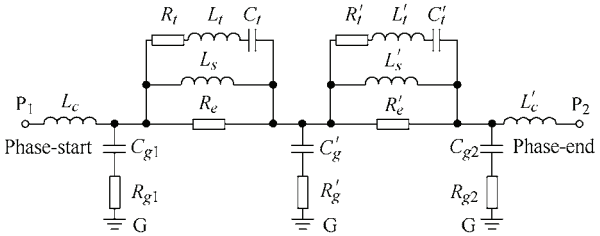

Fig. 3 Per phase equivalent circuit of the proposed model

2.2 Parameterization process

To obtain the values of the circuit elements in Fig. 3, the motor per phase impedances, namely, the phase-start to phase-end impedance ($Z_{P_1P_2}$), phase-start to ground impedance (Z_{P_1G}), and phase-end to ground impedance (Z_{P_2G}), are used in an artificial neural network.

As illustrated in Fig. 4, the neural network consists of six layers: one input layer, four hidden layers, and one output layer. The input is a random constant (C). The output are the predicted values of the eighteen circuit elements per phase. The number of neurons in the four hidden layers are set as 50, 200, 200, and 50, respectively. The loss function (g_L) per phase is defined as follows

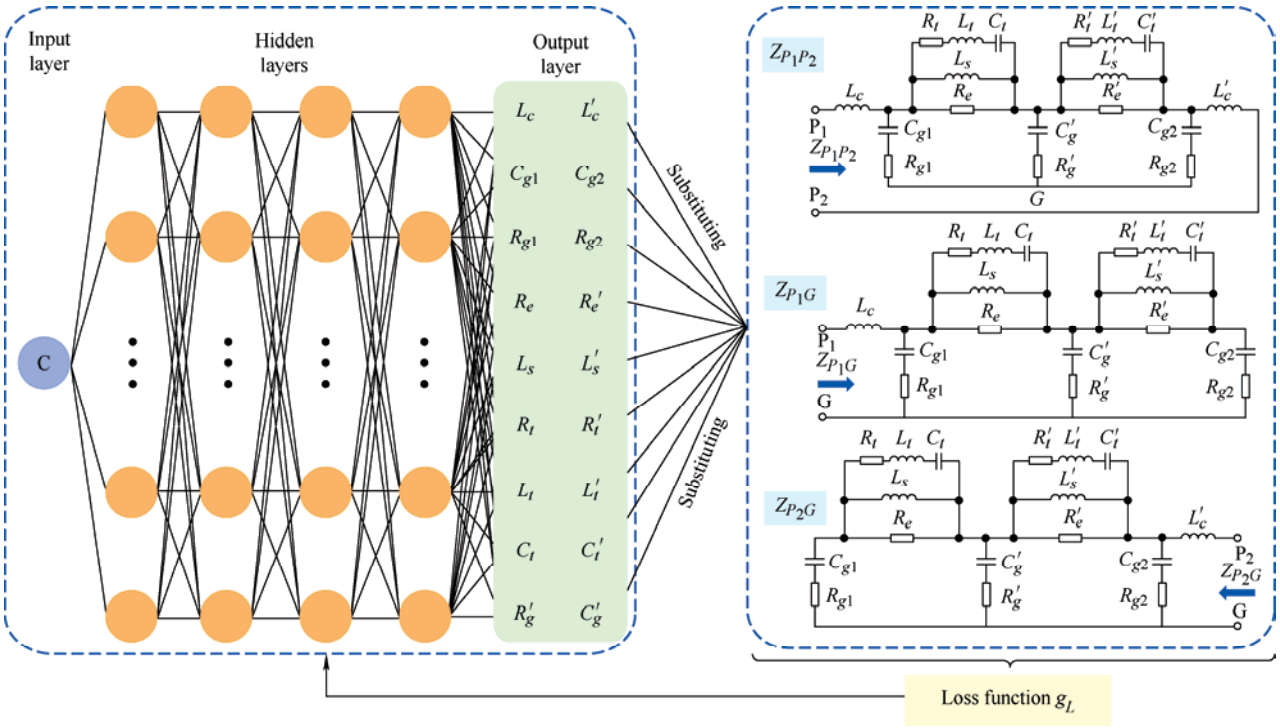

Fig. 4 Physics informed neural network to obtain circuit elements per phase

$$g_L = \frac{g_L\left(|Z|\right)+g_L\left(\angle Z\right)}{2} \tag{1}$$

$$g_L\left(|Z|\right)=\frac{g_L\left(\left|Z_{P_1P_2}\right|\right)+g_L\left(\left|Z_{P_1G}\right|\right)+g_L\left(\left|Z_{P_2G}\right|\right)}{3} \tag{2}$$

$$g_L\left(\angle Z\right)=\frac{g_L\left(\angle Z_{P_1P_2}\right)+g_L\left(\angle Z_{P_1G}\right)+g_L\left(\angle Z_{P_2G}\right)}{3} \tag{3}$$

$$g_L\left(\left|Z_{P_1P_2}\right|\right)=\frac{1}{n}\sum_{i=1}^{n}\lg\left[\cosh\left(1-\frac{\left|\tilde{Z}_{P_1P_2}\right|}{\left|Z_{P_1P_2}\right|}\right)\right] \tag{4}$$

$$g_L\left(\left|Z_{P_1G}\right|\right)=\frac{1}{n}\sum_{i=1}^{n}\lg\left[\cosh\left(1-\frac{\left|\tilde{Z}_{P_1G}\right|}{\left|Z_{P_1G}\right|}\right)\right] \tag{5}$$

$$g_L\left(\left|Z_{P_2G}\right|\right)=\frac{1}{n}\sum_{i=1}^{n}\lg\left[\cosh\left(1-\frac{\left|\tilde{Z}_{P_2G}\right|}{\left|Z_{P_2G}\right|}\right)\right] \tag{6}$$

$$g_L\left(\angle Z_{P_1P_2}\right)=\frac{1}{n}\sum_{i=1}^{n}\lg\left[\cosh\left(1-\frac{\angle\tilde{Z}_{P_1P_2}+\Delta}{\angle Z_{P_1P_2}+\Delta}\right)\right] \tag{7}$$

$$g_L\left(\angle Z_{P_1G}\right)=\frac{1}{n}\sum_{i=1}^{n}\lg\left[\cosh\left(1-\frac{\angle\tilde{Z}_{P_1G}+\Delta}{\angle Z_{P_1G}+\Delta}\right)\right] \tag{8}$$

$$g_L\left(\angle Z_{P_2G}\right)=\frac{1}{n}\sum_{i=1}^{n}\lg\left[\cosh\left(1-\frac{\angle\tilde{Z}_{P_2G}+\Delta}{\angle Z_{P_2G}+\Delta}\right)\right] \tag{9}$$

where $Z_{P_1P_2}$, Z_{P_1G}, and Z_{P_2G} can be measured using a high-precision impedance analyzer in the frequency range of interest (i.e., 1 kHz-30 MHz). $\tilde{Z}_{P_1P_2}$, $\tilde{Z}_{P_1G}$, and $\tilde{Z}_{P_2G}$ denote estimated values with the neural network. n is the number of frequency points in the frequency range of interest.

As seen in Eqs. (1)-(9), the loss function (g_L) for per phase training includes a magnitude loss $g_L\left(|Z|\right)$ and a phase loss $g_L\left(\angle Z\right)$. The magnitude loss components $g_L\left(\left|Z_{P_1P_2}\right|\right)$, $g_L\left(\left|Z_{P_1G}\right|\right)$, and $g_L\left(\left|Z_{P_2G}\right|\right)$ are directly derived from their respective relative error between the estimated and measured values. The pointwise mean of log-cosh function is applied to equally consider the magnitude errors of all frequency points. On the other hand, the phase loss components $g_L\left(\angle Z_{P_1P_2}\right)$, $g_L\left(\angle Z_{P_1G}\right)$, and $g_L\left(\angle Z_{P_2G}\right)$ incorporate the same shift Δ ($\Delta > 90°$) on the estimated and measured values before loss calculation. The phase shift is to avoid division by zero for a stable and smooth training process. By minimizing g_L, the values of the circuit elements per phase can be determined. Finally, the three-phase equivalent circuit can be constructed based on the corresponding motor

connection (star or delta).

Fig. 5 shows a flowchart of the parameterization process. It illustrates how the estimated impedances with the circuit elements generated by the neural network are compared with the corresponding measured impedances. The magnitude and phase errors between the estimated and measured impedances are calculated with Eqs. (4)-(9) to update the value of the loss function (g_L). If the termination criteria are reached (i.e., stop condition), the set of values of the circuit elements are accepted to produce the optimized model; otherwise, the aforementioned steps are repeated.

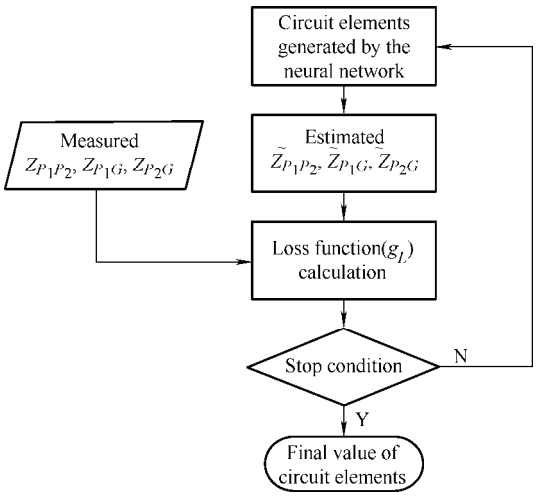

Fig. 5 Flowchart of parameterization process

For proof of concept, a 5.5 kW induction motor (TEOC AEEBKB067R50FM) is selected as the case study. Since the rotor speed and stator current have no significant influence on the motor impedance characteristics in mid-to-high frequency range [10], $Z_{P_1P_2}$, Z_{P_1G}, and Z_{P_2G} for all three phases are measured offline using a Keysight E4990A impedance analyzer in the range of 1 kHz-30 MHz. The number of frequency points n is set to 1186. The frequency points are logarithmically distributed from 1 kHz to 30 MHz. An 8 core 2.40-GHz PC is used as the parameterization platform. The stop condition of parameterization is set that the mean absolute relative error of $|Z_{P_1P_2}|$, $|Z_{P_1G}|$, and $|Z_{P_2G}|$ are reduced to 1.5 dB, and the mean absolute error of $\angle Z_{P_1P_2}$, $\angle Z_{P_1G}$, and $\angle Z_{P_2G}$ are reduced to 9.0°. The parameterization time for all three phases is around 5 minutes.

Fig. 6 shows the measured $Z_{P_1P_2}$, Z_{P_1G}, and Z_{P_2G} and the estimated $\tilde{Z}_{P_1P_2}$, $\tilde{Z}_{P_1G}$, and $\tilde{Z}_{P_2G}$ for phase A of the 5.5 kW induction motor in the range of 1 kHz-30 MHz. Similarly, Figs. 7 and 8 show the measured and estimated results for phases B and C in the same frequency range, respectively. As observed, the estimated $\tilde{Z}_{P_1P_2}$, $\tilde{Z}_{P_1G}$, and $\tilde{Z}_{P_2G}$ have demonstrated good agreement with the measured $Z_{P_1P_2}$, Z_{P_1G}, and Z_{P_2G} in both their magnitudes and phases for all three phases of the induction motor over the range of 1 kHz-30 MHz. Tab. 1 lists the estimated values of the circuit elements for all three phases of the 5.5 kW induction motor. Thus, the motor three-phase equivalent circuit can be constructed based on these circuit elements and the corresponding motor connection (star or delta).

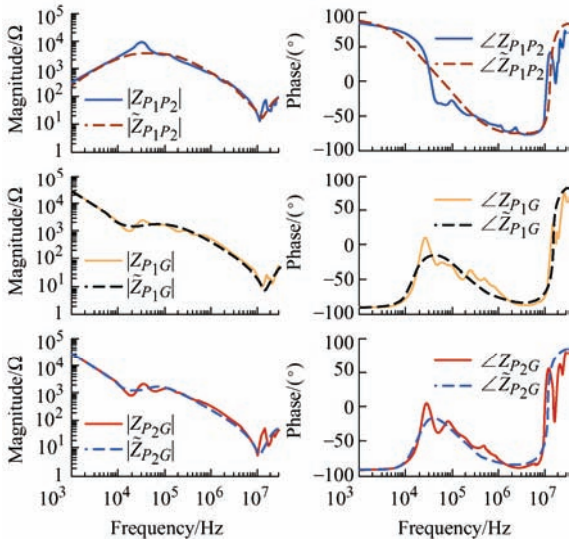

Fig. 6 Measured $Z_{P_1P_2}$, Z_{P_1G}, and Z_{P_2G} and estimated $\tilde{Z}_{P_1P_2}$, $\tilde{Z}_{P_1G}$, and $\tilde{Z}_{P_2G}$ for phase A of the 5.5 kW induction motor

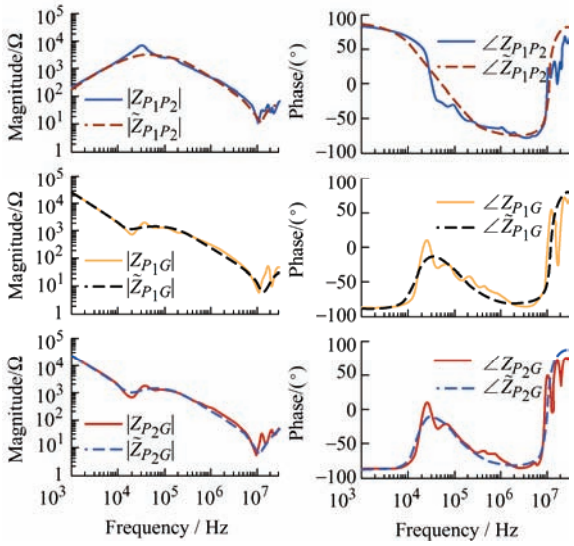

Fig. 7 Measured $Z_{P_1P_2}$, Z_{P_1G}, and Z_{P_2G} and estimated $\tilde{Z}_{P_1P_2}$, $\tilde{Z}_{P_1G}$, and $\tilde{Z}_{P_2G}$ for phase B of the 5.5 kW induction motor

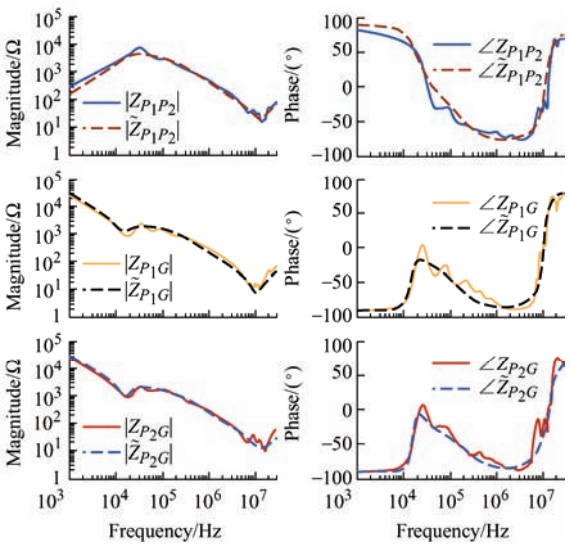

Fig. 8 Measured $Z_{P_1P_2}$, Z_{P_1G}, and Z_{P_2G} and estimated $\tilde{Z}_{P_1P_2}$, $\tilde{Z}_{P_1G}$, and $\tilde{Z}_{P_2G}$ for phase C of the 5.5 kW induction motor

Tab. 1 Estimated values of circuit elements for all three phases of the 5.5 kW induction motor

Element	A	B	C	Element	A	B	C
L_c/μH	0.28	0.25	0.30	L_c' /μH	0.31	0.33	0.20
C_{g1}/pF	426	568	691	C_{g2}/pF	631	631	601
R_{g1}/Ω	6.52	6.77	7.84	R_{g2}/Ω	5.38	5.98	12.5
R_e/kΩ	1.82	1.86	8.71	R_e' /kΩ	1.80	1.98	14.2
L_s/mH	20.5	18.1	15.3	L_s' /mH	16.0	15.5	12.4
R_t/kΩ	43.2	42.6	2.93	R_t' /kΩ	37.8	42.8	2.30
L_t/mH	10.3	41.6	0.94	L_t' /mH	11.1	40.7	0.34
C_t/pF	2.75	2.55	3.98	C_t' /pF	2.76	2.54	3.29
R_g' /Ω	50.8	58.4	201	C_g' /nF	4.92	4.84	3.83

3 Experimental validation

For the experimental validation, the same 5.5 kW induction motor is selected as the case study. To verify the accuracy of the constructed circuit model for predicting the motor CM and DM impedances under both star and delta connections ($Z_{CM\text{-}Y}$, $Z_{DM\text{-}Y}$, $Z_{CM\text{-}\Delta}$, $Z_{DM\text{-}\Delta}$), the actual measurement results are used as references for comparison. Fig. 9 shows the configuration for measuring $Z_{CM\text{-}Y}$, $Z_{DM\text{-}Y}$, $Z_{CM\text{-}\Delta}$ and $Z_{DM\text{-}\Delta}$ using a Keysight E4990A impedance analyzer.

Based on the obtained values of the circuit elements for all three phases listed in Tab. 1, Fig. 10 shows the simulated $Z_{CM\text{-}Y}$ and $Z_{DM\text{-}Y}$ in the range of 1 kHz-30 MHz. Similarly, Fig. 11 shows the simulated $Z_{CM\text{-}\Delta}$ and $Z_{DM\text{-}\Delta}$ values in the same frequency range. The measured results are shown in the same figures for comparison. As observed, both the magnitude and phase of the simulated $Z_{CM\text{-}Y}$, $Z_{DM\text{-}Y}$, $Z_{CM\text{-}\Delta}$ and $Z_{DM\text{-}\Delta}$ are in good agreement with the measured results over the range of 1 kHz-30 MHz. To quantify this agreement, using the measured results as references, Tab. 2 lists the mean absolute relative error (MARE) of $|Z_{CM\text{-}Y}|$, $|Z_{DM\text{-}Y}|$, $|Z_{CM\text{-}\Delta}|$ and $|Z_{DM\text{-}\Delta}|$, as well as the mean absolute error (MAE) of $\angle Z_{CM\text{-}Y}$, $\angle Z_{DM\text{-}Y}$, $\angle Z_{CM\text{-}\Delta}$ and $\angle Z_{DM\text{-}\Delta}$.

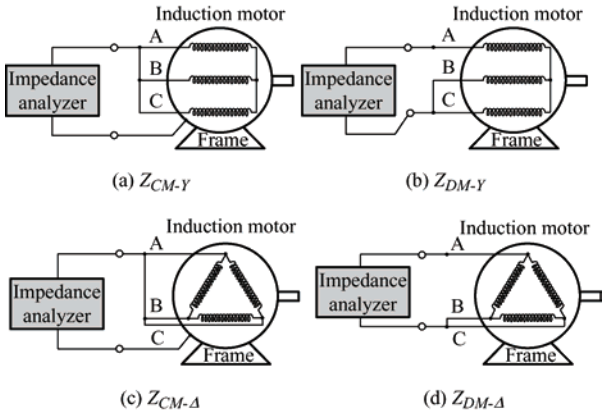

Fig. 9 Configuration for measuring motor impedances

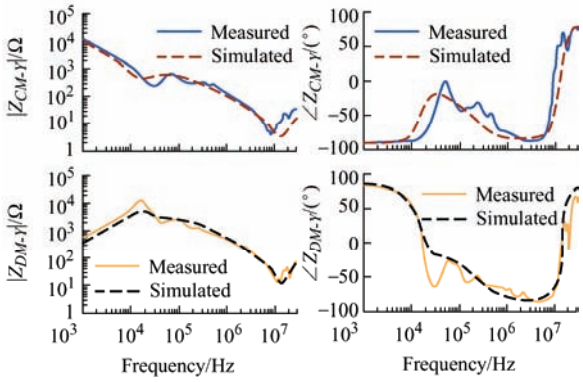

Fig. 10 Measured and simulated $Z_{CM\text{-}Y}$ and $Z_{DM\text{-}Y}$ of the 5.5 kW induction motor

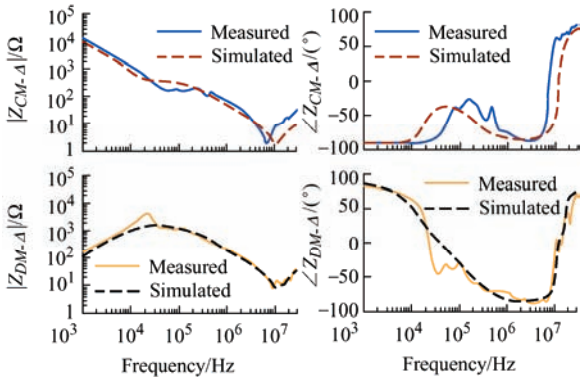

Fig. 11 Measured and simulated $Z_{CM\text{-}\Delta}$ and $Z_{DM\text{-}\Delta}$ of the 5.5 kW induction motor

As presented in Tab. 2, the maximum MARE and MAE are 2.8 dB and 13.9° , respectively. With Figs. 10 and 11, as well as Tab. 2, the high accuracy of the

proposed HF modeling method for predicting the motor CM and DM impedances over the range of 1 kHz-30 MHz is validated. In addition, its good versatility that is applicable to both star- and delta-connected induction motors without having to recalculate the circuit element values when changing the motor connections is also demonstrated.

Tab. 2 Errors of the simulation results

Magnitude	MARE/dB	Phase	MAE/(°)
$\lvert Z_{CM\text{-}Y}\rvert$	2.4	$\angle Z_{CM\text{-}Y}$	12.5
$\lvert Z_{DM\text{-}Y}\rvert$	2.3	$\angle Z_{DM\text{-}Y}$	13.9
$\lvert Z_{CM\text{-}\Delta}\rvert$	2.8	$\angle Z_{CM\text{-}\Delta}$	11.4
$\lvert Z_{DM\text{-}\Delta}\rvert$	1.8	$\angle Z_{DM\text{-}\Delta}$	13.5

4 Conclusions

This study proposed a physics informed neural network-based HF modeling method for induction motors with the advantages of high accuracy, good versatility, and simple parameterization. The proposed model consists of eighteen circuit elements per phase with a symmetric structure, which is applicable to both star- and delta-connected induction motors. In addition, it does not need to recalculate the circuit element values when changing the motor connections. Three per-phase impedances (phase-start to phase-end, phase-start to ground, and phase-end to ground) are used in the artificial neural network to obtain the values of the circuit elements in each phase. The parameterization could be easily implemented within a few minutes using a common PC. Using a 5.5 kW induction motor as the case study, the experimental results have demonstrated the effectiveness of the proposed HF modeling method, as well as its good accuracy for predicting motor CM and DM impedances under both star and delta connections in the range of 1 kHz-30 MHz, which promises an accurate prediction of the overvoltage and conducted emissions. The proposed modeling method is not only applicable to induction motors but also to other types of motors, such as permanent magnet synchronous motors and brushless DC motors.

References

[1] S Amarir, K Al-Haddad. A modeling technique to analyze the impact of inverter supply voltage and cable length on industrial motor-drives. *IEEE Trans. Power Electron.*, 2008, 23(2): 753-762.

[2] G Skibinski, R Kerkman, D Leggate, et al. Reflected wave modeling techniques for PWM AC motor drives. *Proc. Appl. Power Electron. Conf. (APEC)*, February 15-19, 1998, Anaheim, CA, USA. IEEE, 1998: 1021-1029.

[3] M Ghassemi. Accelerated insulation aging due to fast, repetitive voltages: A review identifying challenges and future research needs. *IEEE Trans. Dielectr. Electr. Insul.,* 2019, 26(5): 1558-1568.

[4] Z Yang, H Li, Z Yang, et al. Conducted electromagnetic interference analysis method for traction drive system in high speed trains. *2017 IEEE Transp. Electrific. Conf. Expo*, *Asia-Pacific*, August 7-10, 2017, Harbin, China. IEEE, 2017: 1-5.

[5] Z Zhang, Y Hu, X Chen, et al. A review on conductive common-mode EMI suppression methods in inverter fed motor drives. *IEEE Access*, 2021, 9: 18345-18360.

[6] G Grandi, D Casadei, U Reggiani. Common- and differential-mode HF current components in AC motors supplied by voltage source inverters. *IEEE Trans. Power Electron.*, 2004, 19(1): 16-24.

[7] Z Yang, H Li, C Feng, et al. Survey on electromagnetic interference analysis for traction converters in railway vehicles. *Proc. IEEE Int. Power Electron. Conf.*, May 20-24, 2018, Niigata, Japan. IEEE, 2018: 2058-2065.

[8] L Ran, S Gokani, J Clare, et al. Conducted electromagnetic emissions in induction motor drive systems I: Time domain analysis and identification of dominant modes. *IEEE Trans. Power Electron.*, 1998, 13(4): 757-767.

[9] M M Swamy, K Yamada, T Kume. Common mode current attenuation techniques for use with PWM drives. *IEEE Trans. Power Electron.*, 2001, 16(2): 248-255.

[10] L Wang, C N Ho, F Canales, et al. High-frequency modeling of the long-cable-fed induction motor drive system using TLM approach for predicting overvoltage transients. *IEEE Trans. Power Electron.*, 2010, 25(10): 2653-2664.

[11] G Suresh, A Toliyat, A Rendusara, et al. Predicting the transient effects of PWM voltage waveform on the stator windings of random wound induction motors. *IEEE Trans. Power Electron.*, 1999, 14(1): 23-30.

[12] K Maki, H Funato, L Shao. Motor modeling for EMC simulation by 3-D electromagnetic field analysis. *2009 IEEE International Electric Machines and Drives Conf.*, May 3-6, 2009, Miami, FL, USA. IEEE, 2009: 103-108.

[13] V Mihaila, S Duchesne, D Roger. A simulation method to predict the turn-to-turn voltage spikes in a PWM fed motor winding. *IEEE Trans. Dielectr. Electr. Insul.*, 2011, 18(5): 1609-1615.

[14] Y Ryu, M Yea, J Kim, et al. Stator impedance modeling platform for the electromagnetic compatibility aware design of 3.7-to 7.5-kW squirrel-cage induction motors. *IEEE Trans. Ind. Electron.*, 2021, 68(11): 11255-11265.

[15] L Ran, S Gokani, J Clare, et al. Conducted electromagnetic emissions in induction motor drive systems part II: Frequency domain models. *IEEE Trans. Power Electron.*, 1998, 13(4): 768-776.

[16] F Fan, K Y See, X Liu, et al. Systematic common-mode filter design for inverter-driven motor system based on in-circuit impedance extraction. *IEEE Trans. Electromagn. Compat.*, 2020, 62(5): 1711-1722.

[17] F Costa, C Vollaire, R Meuret. Modeling of conducted common mode perturbations in variable-speed drive systems. *IEEE Trans. Electromagn. Compat.*, 2005, 47(4): 1012-1021.

[18] A F Moreira, T A Lipo, G Venkataramanan, et al. High-frequency modeling for cable and induction motor overvoltage studies in long cable drives. *IEEE Trans. Ind. Appl.*, 2002, 38(5):1297-1306.

[19] A Boglietti, A Cavagnino, M Lazzari. Experimental high-frequency parameter identification of AC electrical motors. *IEEE Trans. Ind. Appl.*, 2007, 43(1): 23-29.

[20] J Sun, L Xing. Parameterization of three-phase electric machine models for EMI simulation. *IEEE Trans. Power Electron.*, 2014, 29(1): 36-41.

[21] M S Toulabi, L Wang, L Bieber, et al. A universal high-frequency induction machine model and characterization method for arbitrary stator winding connections. *IEEE Trans. Energy Convers.*, 2019, 34(3): 1164-1177.

[22] M Schinkel, S Weber, S Guttowski, et al. Efficient HF modeling and model parameterization of induction machines for time and frequency domain simulations. *Proc. IEEE Appl. Power Electron. Conf. Expo. (APEC)*, March 19-23, 2006, Dallas, TX, USA. IEEE, 2006: 1-6.

[23] B Mirafzal, G Skibinski, R Tallam. Determination of parameters in the universal induction motor model. *IEEE Trans. Ind. Appl.*, 2009, 45(1): 142-151.

[24] V Karakaşlı, F Gross, T Braun, et al. High-frequency modeling of delta- and star-connected induction motors. *IEEE Trans. Electromagn. Compat.*, 2022, 64(4): 1533-1544.

[25] M Degano, P Zanchetta, L Empringham, et al. HF induction motor modeling using automated experimental impedance measurement matching. *IEEE Trans. Ind. Electron.*, 2012, 59(10): 3789-3796.

[26] H Chen, S Ye. Modeling of common-mode impedance of an inverter-fed induction motor from online measurement. *IEEE Trans. Electromagn. Compat.*, 2018, 60(5): 1581-1589.

[27] Z Zhao, F Fan, Q Sun, et al. High-frequency modeling of induction motor using multilayer perceptron. *Proc. Asia-Pacific Int. Symp. Electro. Compat.*, September 1-4, 2022, Beijing, China. IEEE, 2022: 222-224.

Zhenyu Zhao (M'21) received the B.Eng. degree in Electrical and Electronic Engineering from Huazhong University of Science and Technology, Wuhan, China, in 2015, and the Ph.D. degree in Electrical and Electronic Engineering from Nanyang Technological University, Singapore, in 2021.

He is a Research Fellow at Nanyang Technological University. His research interests include electromagnetic interference, electromagnetic security, impedance measurements, and electromagnetic sensors. In these areas, he has authored and co-authored more than 50 refereed papers.

Dr. Zhao received 4 awards and 3 award finalists from IEEE, including the Best Student Paper Award at the Joint IEEE EMC & APEMC 2018, the Best Paper Award Finalist at the APEMC 2021, the Young Scientist Award and the Best Paper Award at the APEMC 2022. He was invited to participate in the Global Young Scientists Summit in 2019 and 2022. He has served as a Session Chair/Organizer and a TPC Member for many international conferences. Since 2022, he has been serving as an Executive Committee Member and the Secretary of the IEEE EMC Society, Singapore Chapter.

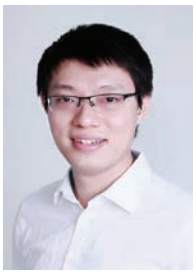

Fei Fan (M'19) received the B.Eng. degree in Electrical Engineering from Tianjin University, Tianjin, China, in 2014, and the M.Sc. in Power Engineering and Ph.D. degrees in Electrical Engineering from Nanyang Technological University (NTU), Singapore, in 2015 and 2020, respectively.

He is currently a Research Fellow in the School of Electrical and Electronic Engineering, NTU. His research interests include electromagnetic compatibility and electromagnetic interference measurement, in-circuit impedance extraction, and EMI filter design for motor drive systems.

Dr. Fan was a recipient of the Best Student Paper Award at the 2017 Asia-Pacific Symposium on Electromagnetic Compatibility (APEMC) and Progress in Electromagnetics Research Symposium (PIERS).

Quqin Sun received the B.Eng. and Ph.D. degrees in Electrical Engineering from Huazhong University of Science and Technology, Wuhan, China. in 2011 and 2016, respectively.

He worked as a Research Associate at the Institute of Fluid Physics of China Academy of Engineering Physics till 2018. From 2018 to 2021, he joined Nanyang Technological University, Singapore, as a Research Fellow. He is now an Engineer in Wuhan Second Ship Design and Research Institute. His research interests include high-field pulsed magnet design, electromagnetic launch, laser-ultrasonic non-destructive inspection, and motor condition monitoring.

Huamin Jie (S'22) received the B.Eng. degree in Electrical Engineering from Wuhan University, Wuhan, China, in 2019, and the M.Sc. degree in Power Engineering from Nanyang Technological University, Singapore, in 2020, respectively. He is currently working toward the Ph.D. degree with the School of Electrical and Electronic Engineering, Nanyang Technological University.

His research interests include impedance measurements, device modeling, electromagnetic interference (EMI), and EMI filter design.

Zhou Shu (M'21) received the B.Sc., M.Eng. and Ph.D. degrees in Integrated Circuit and System from Chongqing University, Chongqing, China, in 2015, 2017, and 2020, respectively.

In 2021, he joined Nanyang Technological University, Singapore, as a Research Fellow. His research interests include mixed-signal integrated circuit design for high-speed wireline links, power management units and low-power sensor interfaces, and testing and fault diagnosis for industrial applications.

Wensong Wang (M'18-SM'22) received the Ph.D. degree in Communication and Information Systems from Nanjing University of Aeronautics and Astronautics, Nanjing, China, in 2016.

From 2013 to 2015, he was a Visiting Scholar with the University of South Carolina, Columbia, USA. In 2017, he joined Nanyang Technological University, Singapore, as a Research Fellow, and now he is a Senior Research Fellow.

His research interests include MIMO antenna, antenna arrays, and advanced sensors.

Kye Yak See (M'86-SM'02) received the B.Eng. degree in Electrical Engineering from National University of Singapore, Singapore, in 1986, and the Ph.D. degree in Electrical Engineering from Imperial College London, UK, in 1997.

From 1986 to 1991, he was with Singapore Technologies Electronics, Singapore, as a Senior Engineer. From 1991 to 1994, he was a lead Design Engineer with ASTEC Custom Power, Singapore. Since 1997, he has been with Nanyang Technological University (NTU), Singapore, as a Faculty Member. He is currently an Associate Professor with the School of Electrical and Electronic Engineering, NTU. He holds concurrent appointment as Director of the Electromagnetic Effects Research Laboratory and Director of SMRT-NTU Smart Urban Rail Corporate Laboratory. His current research interests include electromagnetic compatibility (EMC), signal integrity, and real-time condition monitoring.

Dr. See is the Founding Chairs of the IEEE Electromagnetic Compatibility (EMC) Chapter, IEEE Aerospace and Electronic Systems, and the IEEE Geoscience and Remote Sensing Joint Chapter in Singapore. He was the General Chairs of 2015 Asia Pacific Conference on Synthetic Aperture Radar (APSAR 2015) and 2018 International Conference on Intelligent Rail Transportation (ICIRT 2018). Since January 2012, he has been the Technical Editor of the IEEE Electromagnetic Compatibility Magazine.